Computers in Biology and Medicine 141 (2022) 105145

Contents lists available at ScienceDirect

Computers in Biology and Medicine

journal homepage: www.elsevier.com/locate/compbiomed

Non-contrast Cine Cardiac Magnetic Resonance image radiomics features and machine learning algorithms for myocardial infarction detection

Elham Avard [a,1], Isaac Shiri [b,1], Ghasem Hajianfar [c], Hamid Abdollahi [d], Kiara Rezaei Kalantari [c], Golnaz Houshmand [c], Kianosh Kasani [c], Ahmad Bitarafan-rajabi [c,***], Mohammad Reza Deevband [a,**], Mehrdad Oveisi [e], Habib Zaidi [b,f,g,h,*]

[a] Department of Biomedical Engineering and Medical Physics, Shahid Beheshti University of Medical Sciences, Tehran, Iran
[b] Division of Nuclear Medicine and Molecular Imaging, Geneva University Hospital, CH-1211, Geneva 4, Switzerland
[c] Rajaie Cardiovascular Medical and Research Center, Iran University of Medical Science, Tehran, Iran
[d] Department of Radiologic Sciences and Medical Physics, Faculty of Allied Medicine, Kerman University of Medical Science, Kerman, Iran
[e] Comprehensive Cancer Centre, School of Cancer & Pharmaceutical Sciences, Faculty of Life Sciences & Medicine, King's College London, London, United Kingdom
[f] Geneva University Neurocenter, Geneva University, Geneva, Switzerland
[g] Department of Nuclear Medicine and Molecular Imaging, University of Groningen, University Medical Center Groningen, Groningen, Netherlands
[h] Department of Nuclear Medicine, University of Southern Denmark, Odense, Denmark

ARTICLE INFO

Keywords:
Cine-CMR
Radiomics
Machine learning
Myocardial infarction

ABSTRACT

Objective: Robust differentiation between infarcted and normal tissue is important for clinical diagnosis and precision medicine. The aim of this work is to investigate the radiomic features and to develop a machine learning algorithm for the differentiation of myocardial infarction (MI) and viable tissues/normal cases in the left ventricular myocardium on non-contrast Cine Cardiac Magnetic Resonance (Cine-CMR) images.

Methods: Seventy-two patients (52 with MI and 20 healthy control patients) were enrolled in this study. MR imaging was performed on a 1.5 T MRI using the following parameters: TR = 43.35 ms, TE = 1.22 ms, flip angle = 65°, temporal resolution of 30–40 ms. *N4 bias* field correction algorithm was applied to correct the inhomogeneity of images. All images were segmented and verified simultaneously by two cardiac imaging experts in consensus. Subsequently, features extraction was performed within the whole left ventricular myocardium (3D volume) in end-diastolic volume phase. Re-sampling to $1 \times 1 \times 1$ mm^3 voxels was performed for MR images. All intensities within the VOI of MR images were discretized to 64 bins. Radiomic features were normalized to obtain Z-scores, followed by Student's t-test statistical analysis for comparison. A p-value < 0.05 was used as a threshold for statistically significant differences and false discovery rate (FDR) correction performed to report q-value (FDR adjusted p-value). The extracted features were ranked using the MSVM-RFE algorithm, then Spearman correlation between features was performed to eliminate highly correlated features (R2 > 0.80). Ten different machine learning algorithms were used for classification and different metrics used for evaluation and various parameters used for models' evaluation.

Results: In univariate analysis, the highest area under the curve (AUC) of receiver operating characteristic (ROC) value was achieved for the Maximum 2D diameter slice (M2DS) shape feature (AUC = 0.88, q-value = 1.02E-7), while the average of univariate AUCs was 0.62 ± 0.08. In multivariate analysis, Logistic Regression (AUC = 0.93 ± 0.03, Accuracy = 0.86 ± 0.05, Recall = 0.87 ± 0.1, Precision = 0.93 ± 0.03 and F1 Score = 0.90 ± 0.04) and SVM (AUC = 0.92 ± 0.05, Accuracy = 0.85 ± 0.04, Recall = 0.92 ± 0.01, Precision = 0.88 ± 0.04 and F1 Score = 0.90 ± 0.02) yielded optimal performance as the best machine learning algorithm for this radiomics analysis.

Conclusion: This study demonstrated that using radiomics analysis on non-contrast Cine-CMR images enables to accurately detect MI, which could potentially be used as an alternative diagnostic method for Late Gadolinium Enhancement Cardiac Magnetic Resonance (LGE-CMR).

* Corresponding author. Geneva University Hospital, Division of Nuclear Medicine and Molecular Imaging, CH-1211, Geneva, Switzerland.
** Corresponding author. Department of Medical Physics, School of Medicine, Shahid Beheshti University of Medical Sciences, Tehran, Iran.
*** Corresponding author. Rajaie Cardiovascular Medical and Research Center, Iran University of Medical Science, Tehran, Iran.
E-mail addresses: bitarafan@hotmail.com (A. Bitarafan-rajabi), mdeevband@sbmu.ac.ir (M.R. Deevband), habib.zaidi@hcuge.ch (H. Zaidi).
[1] Elham Avard and Isaac Shiri have contributed equally to this manuscript.

https://doi.org/10.1016/j.compbiomed.2021.105145
Received 8 December 2021; Accepted 13 December 2021
Available online 15 December 2021
0010-4825/© 2021 The Author(s). Published by Elsevier Ltd. This is an open access article under the CC BY-NC-ND license (http://creativecommons.org/licenses/by-nc-nd/4.0/).

1. Introduction

The worldwide prevalence of cardiovascular disease (CVD) in adults older than 20 years in 2018 is 49.2% (126.9 million people) and increases with age [1]. CVD affects different parts of the heart and induce structural and functional complications [2]. Cardiac ischemia, which is characterized by reduced blood flow and oxygen to the heart, could trigger myocardial infarction (MI) [3,4]. Therefore, the ventricular myocardium loses part of its functions, a state commonly referred to as infarcted myocardium [3,4]. According to previous studies, parameters including systolic function and ventricular volumes could be used as main predictive markers of MI consequences [2,5]. To this end, diagnostic methods, including transthoracic echocardiography and Cardiac Magnetic Resonance (CMR) are fast, reproducible, accurate and widely available approaches to evaluate these parameters. Furthermore, single-photon emission tomography (SPECT), positron emission tomography (PET) and computed tomography (CT) imaging modalities proved to be clinically relevant approaches for cardiac malfunctions detection and diagnosis [6].

Clinical evidence seems to indicate that the precise assessment of the location and size of infarction is important for prognosis and provides more accurate information to guide critical therapeutic strategies, such as implanting implantable cardioverter-defibrillators [7]. As a feasible diagnostic approach, CMR imaging has been used to examine the viability of left ventricular myocardium muscles [8]. Late Gadolinium Enhancement CMR (LGE-CMR) could determine the infarction. Conversely, LGE is more sensitive than nuclear medicine (SPECT and PET) for MI detection according to some previous studies [9–11]. Considering this evidence, LGE-CMR was introduced as a key clinical approach to assess MI location and size. A number of studies have reported that visual assessment of LGE-CMR is the standard method for the diagnosis of MI [8,12]. However, this method bears some inherent limitations, including the dependence on physician's subjective assessment and intra-observer variability. In addition, the injection of Gadolinium (Gd) to patients with severe renal disease could lead to nephrogenic systemic fibrosis [13], an important issue in clinical setting because of the frequency of coexisting of kidney disease and CVDs in patients [14]. Recent studies used unenhanced Cine-CMR images as an alternative to LGE-CMR to enable reading diagnosing CVDs without Gd injection. Baesler et al. [15] compared the performance of Cine-CMR and LGE-CMR for subacute and chronic MI using radiomic features of 180 patients (120 MI cases and 60 control subjects). Using logistic regression classifier, they demonstrated that non-contrast Cine-CMR is capable of differentiating between normal and subacute and chronic MI. Zhang et al. [16] evaluated the diagnostic capability of Cine-CMR using deep learning algorithms. Their deep learning framework could diagnose the presence of MI (AUC of 0.94) and detect the position and delineate MI in 299 patients (212 MI cases and 87 control subjects).

Furthermore, radiomics and machine learning-based imaging biomarker discovery brought new horizons for more accurate detection, diagnosis, prediction, and prognostication [17–20]. This is an advanced image processing approach enabling the correlation of mineable imaging data to biological and clinical parameters [21–25]. Radiomic features have great potential to translate imaging data to acceptable clinical models, including diagnostic, prognostic, and predictive models [26–32]. Radiomics analysis was recently investigated in the context of CVD, where its ability to identify left ventricular hypertrophy, high and low risk of post MI arrhythmia, and to differentiate between acute, subacute and chronic MI, and myocarditis and healthy myocardium tissue was demonstrated [15,33–36].

The detection of infarcted tissue is important for clinical decision making since any medical or surgical intervention would not be of value in the dead myocardium because no improvement in the function can be expected. The detection of non-infarcted tissue would be the main target of any intervention, including medical or surgical procedures, such as coronary bypass graft [37,38]. As mentioned earlier, robust differentiation between MI and normal tissue is important for clinical diagnosis and precision medicine [39]. Currently, manual, and semi-manual methods are used for MI detection from LGE-CMR examinations. More recently, different machine and deep learning algorithms have been developed for cardiac segmentation [39–43]. The aim of this work is to investigate the radiomic features and to develop a machine learning algorithm to differentiate MI and viable tissues/normal cases in the left ventricular myocardium on non-contrast Cine-CMR images.

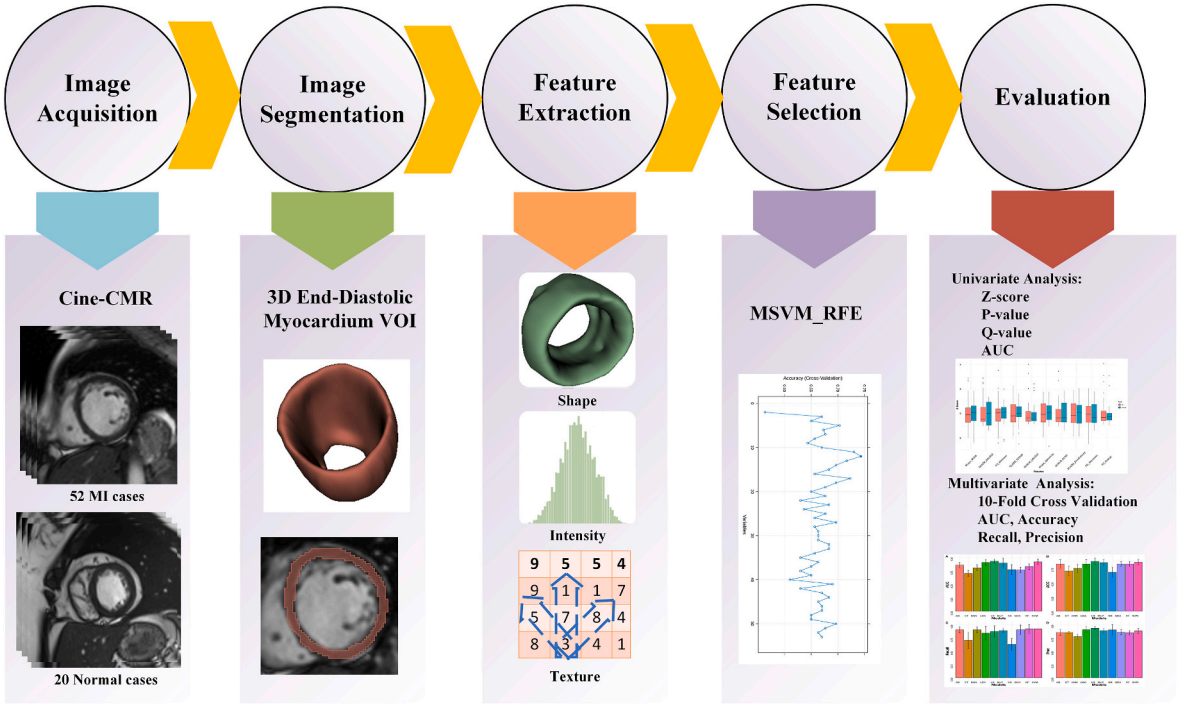

Fig. 1. Flowchart describing the different steps involved in the current study design.

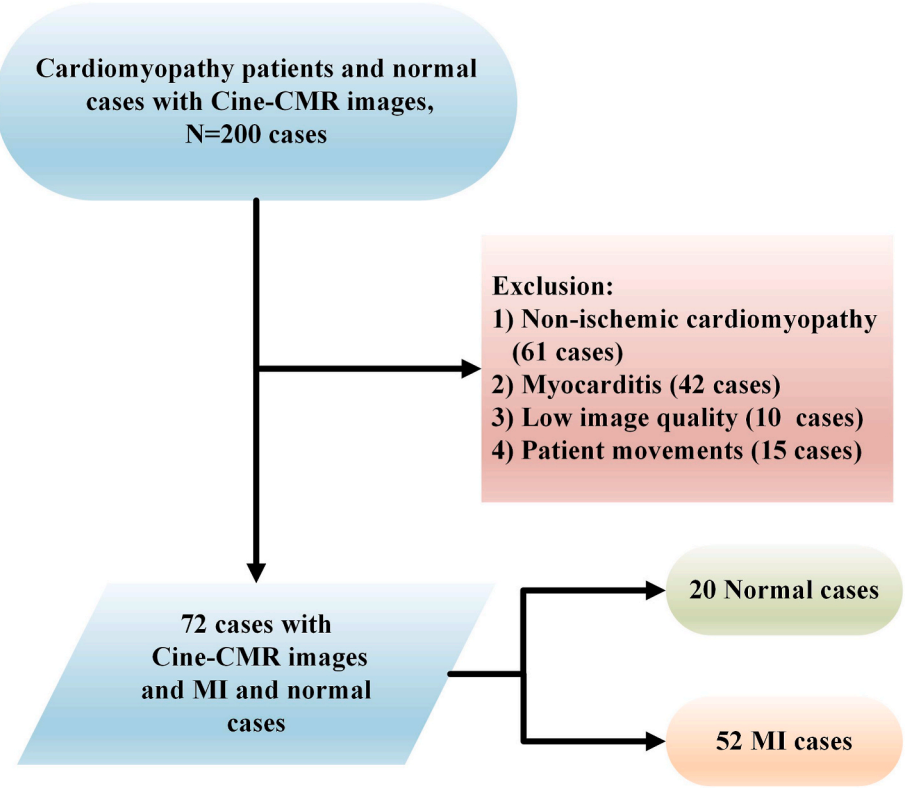

Fig. 2. Flowchart of inclusion and exclusion criteria.

2. Materials and methods

Radiomics analysis included different steps as shown in Fig. 1 and elaborated in the following sections.

2.1. Study population

This study was conducted in accordance with international ethical standards considering the institutional recommendations and the 1964 Helsinki declaration and its later amendments. The protocol was approved by the ethics committee of Shahid Beheshti University of Medical Sciences (No. IR.SBMU.MSP.REC.1398.811). Informed consent was waived owing to the retrospective nature of the study (no impact on clinical diagnosis or patient management). This work involved patients referred by cardiovascular specialist to radiology department to acquire CMR images for viability assessment. To conduct this study, 200 clinical studies were reviewed and cardiomyopathy patients with available Cine-CMR in which different range of transmurality (low to high) can be seen were included. Therefore, infarcted tissue is present in the left ventricle of these ischemic patients. However, those experiencing non-ischemic cardiomyopathy (61 cases) and myocarditis (42 cases) were excluded. Since their symptoms may be similar to MI, they might mistakenly be considered as MI cases, hence impacting accurate diagnosis. We also excluded 25 cases because of low image quality or patient movement. In addition, 20 healthy subjects were considered as normal group. After applying inclusion and exclusion criteria, 72 patients including 52 MI (LGE-CMR images of patients considered as gold standard) and 20 normal cases were included. Fig. 2 summarizes inclusion and exclusion criteria adopted in this study protocol.

2.2. MR image acquisition

MR imaging was performed on a 1.5 T MRI scanner (MAGNETOM Aera; Siemens Healthcare) using the following parameters: TR = 43.35 ms, TE = 1.22 ms, flip angle 65°, temporal resolution 30–40 ms parameters. Gated cine images were acquired using a balanced steady-state free precession pulse sequence in short-axis view, covering the LV from the base to apex. Image resolution varied from 1.37 to 1.68 mm^2/pixel.

2.3. Volume of interest definition

All images were segmented and verified simultaneously by two cardiac imaging experts (with 6 and 10 years of experience in cardiovascular imaging) in consensus using the 3D Slicer software [44]. As depicted in Fig. 1, the whole left ventricular myocardium was selected as a volume of interest (VOI) in the end diastolic volume of Cine-CMR images. Overall, 72 VOIs were defined for the 72 patients. In addition, for a better understanding of MI cases, Supplementary Figs. 1–4 show three Cine slices of infarcted cases compared with their corresponding LGE slices and with the MI labeled LGE slices.

2.4. Preprocessing and feature extraction

It is a prerequisite to normalize the images to obtain comparable features from different Cine-CMR images. In the pre-processing step, *N4 bias* field correction algorithm was applied to correct the inhomogeneity of images [45]. Subsequently, features extraction was performed in the whole left ventricular myocardium (3D volume) in end-diastolic volume phase. Radiomic features extraction was performed using the Pyradiomics image biomarker standardization initiative (IBSI) consensus python library [46]. Re-sampling to $1 \times 1 \times 1$ mm^3 was performed for MR images (interpolation using sitkBSpline B-Spline with order 3 interpolation). All intensities within the VOI of MR images were discretized to 64 bins. These features included intensity-based, texture-based and shape-based features. One hundred and seven features were extracted whose characteristics are summarized in Table 1. These features potentially describe the tissue structure of the myocardium through assessing gray-level values of Cine-CMR images to compute

Table 1
Radiomic features included in the current study.

First Order Statistics (FO)	Gray Level Co-occurrence Matrix (GLCM)	Gray Level Run Length Matrix (GLRLM)
Energy	Autocorrelation	Short Run Emphasis (SRE)
Total Energy	Joint Average	Long Run Emphasis (LRE)
Entropy	Cluster Prominence	Gray Level Non-Uniformity (GLN)
Minimum	Cluster Shade	Gray Level Non-Uniformity Normalized (GLNN)
10th percentile	Cluster Tendency	Run Length Non-Uniformity (RLN)
90th percentile	Contrast	Run Length Non-Uniformity Normalized (RLNN)
Maximum	Correlation	Run Percentage (RP)
Mean	Difference Average	Gray Level Variance (GLV)
Median	Difference Entropy	Run Variance (RV)
Interquartile Range	Difference Variance	Run Entropy (RE)
Range	Joint Energy	Low Gray Level Run Emphasis (LGLRE)
Mean Absolute Deviation (MAD)	Joint Entropy	High Gray Level Run Emphasis (HGLRE)
Robust Mean Absolute Deviation (rMAD)	Informal Measure of Correlation (IMC) 1	Short Run Low Gray Level Emphasis (SRLGLE)
Root Mean Squared (RMS)	Informal Measure of Correlation (IMC) 2	Short Run High Gray Level Emphasis (SRHGLE)
Standard Deviation	Inverse Difference Moment (IDM)	Long Run Low Gray Level Emphasis (LRLGLE)
Skewness	Inverse Difference Moment Normalized (IDMN)	Long Run High Gray Level Emphasis (LRHGLE)
Kurtosis	Inverse Difference (ID)	**Gray Level Dependence Matrix (GLDM)**
Variance	Inverse Difference Normalized (IDN)	Small Dependence Emphasis (SDE)
Uniformity	Inverse Variance	Large Dependence Emphasis (LDE)
	Maximum Probability	Gray Level Non-Uniformity (GLN)
	Sum Average	Dependence Non-Uniformity (DN)
	Sum Entropy	Dependence Non-Uniformity Normalized (DNN)
	Sum of Squares	Gray Level Variance (GLV)
Shape Features	**Gray Level Size Zone Matrix (GLSZM)**	Dependence Variance (DV)
Volume	Small Area Emphasis (SAE)	Dependence Entropy (DE)
Surface Area	Large Area Emphasis (LAE)	Low Gray Level Emphasis (LGLE)
Surface Area to Volume ratio	Gray Level Non-Uniformity (GLN)	High Gray Level Emphasis (HGLE)
Sphericity	Gray Level Non-Uniformity Normalized (GLNN)	Small Dependence Low Gray Level Emphasis (SDLGLE)
Spherical Disproportion	Size-Zone Non-Uniformity (SZN)	Small Dependence High Gray Level Emphasis (SDHGLE)
Maximum 3D diameter	Size-Zone Non-Uniformity Normalized (SZNN)	Large Dependence Low Gray Level Emphasis (LDLGLE)
Maximum 2D diameter (Slice) (M2DS)	Zone Percentage	Large Dependence High Gray Level Emphasis (LDHGLE)
Maximum 2D diameter (Column) (M2DC)	Gray Level Variance (GLV)	**Neighboring Gray Tone Difference Matrix (NGTDM)**
Maximum 2D diameter (M2D)	Zone Variance	Coarseness
Major Axis	Zone Entropy (ZE)	Contrast
Minor Axis	Low Gray Level Zone Emphasis (LGLZE)	Busyness
Least Axis	High Gray Level Zone Emphasis (HGLZE)	Complexity
Elongation	Small Area Low Gray Level Emphasis (SALGLE)	Strength
Flatness	Small Area High Gray Level Emphasis (SAHGLE)	
	Large Area Low Gray Level Emphasis (LALGLE)	
	Large Area High Gray Level Emphasis (LAHGLE)	

Table 2
Summary of area under the curve (AUC), p-value and q-value of the top 10 univariate radiomics features after elimination of highly correlated features ($R^2 > 0.80$).

Type	Feature's Name	AUC	p-value	q-value	MI (mean ± SD)	Normal (mean ± SD)
SHAPE	Maximum 2D Diameter Slice	0.885	1.02E-8	1.02E-7	87.7 ± 9.30	76.1 ± 5.28
GLSZM	Small Area Low Gray Level Emphasis	0.786	8.49E-4	1.41E-3	0.220 ± 0.145	0.375 ± 0.164
FO	Minimum	0.781	2.59E-3	3.70E-3	−0.927 ± 0.158	−0.778 ± 0.178
GLSZM	Size Zone Non-Uniformity Normalized	0.779	3.74E-5	1.87E-4	0.248 ± 0.073	0.324 ± 0.057
GLRLM	Long Run Low Gray Level Emphasis	0.771	6.02E-4	1.41E-3	11.8 ± 9.52	6.04 ± 4.10
SHAPE	Sphericity	0.747	9.80E-5	3.26E-4	0.278 ± 0.031	0.304 ± 0.019
GLRLM	Run Length Non-Uniformity	0.712	7.25E-4	1.41E-3	1200 ± 717	788 ± 271
GLSZM	Zone Entropy	0.702	3.21E-3	4.01E-3	2.97 ± 0.452	2.65 ± 0.37
FO	Skewness	0.692	7.25E-3	8.06E-3	1.00 ± 0.67	0.548 ± 0.592
FO	Energy	0.690	9.20E-2	9.21E-2	1445 ± 1156	995 ± 924

texture matrices, including GLCM, GLSZM, GLRLM, NGTDM and GLDM. Therefore, radiomic features are used in this work to potentially recognize changes in the cardiac tissue after myocardial infarction, which is not possible by naked eyes [15,22,23,47].

2.5. Univariate analysis

Radiomic features were normalized to obtain Z-scores, followed by Student's t-test statistical analysis for comparison. Student's t-test was used to indicate statistically significant differences between MI and normal cases for radiomic features extracted from Cine-CMR images. A p-value < 0.05 was used as a threshold for statistically significant differences and false discovery rate (FDR) correction performed to report q-value (FDR adjusted p-value). Univariate analysis and statistical tests were implemented using the R 3.6.3 package.

2.6. Multivariate analysis

2.6.1. Feature selection and classification

In this work, multiple support vector machine recursive feature elimination (MSVM-RFE) was used for automatic feature selection [48]. In this algorithm, a support vector machine (SVM) was trained recursively to rank all features. In each iteration, the features with the smallest ranked score were removed. First, the extracted features were ranked using the MSVM-RFE algorithm, then Spearman correlation between features was performed to eliminate highly correlated features ($R^2 > 0.80$). Different models, including Logistic Regression (LR) as linear model, Linear Discriminant Analysis (LDA) and Quadratic Discriminant Analysis (QDA) as discriminant analysis models, Extra Tree (ET), Random Forest (RF) and AdaBoost (AB) as ensemble methods, k-nearest neighbors (KNN) as an instance-based model, Naive Bayes (NB) as a probabilistic classifier, Linear Support Vector Machine (SVM) and finally Multi-Layer Perceptron (MLP) as a neural network method, were used in the current study. The scikit-learn library [49] was used to implement multivariate analysis.

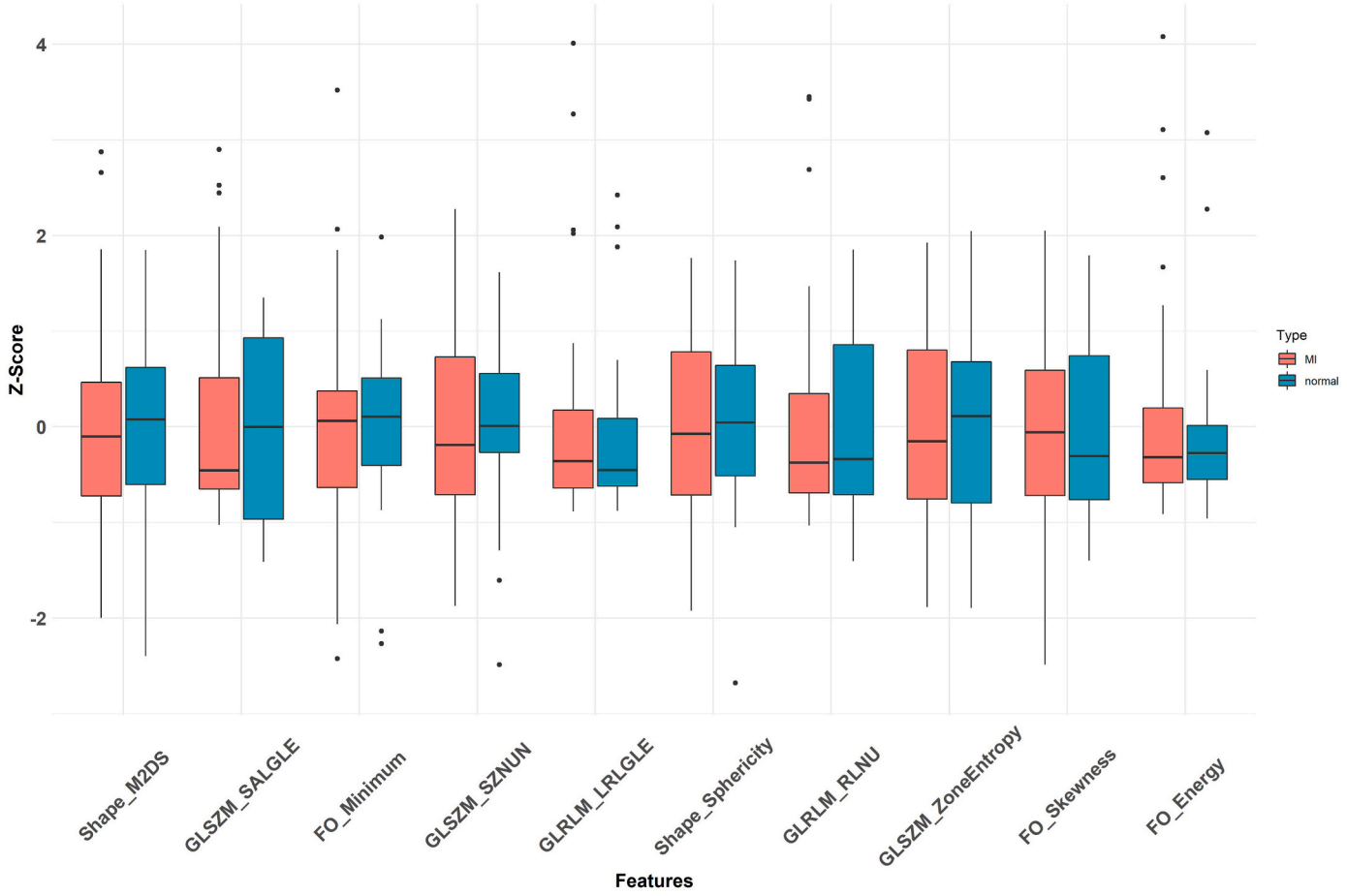

Fig. 3. Box plot of Z-score of univariate analysis of radiomic features.

2.7. Model evaluation

Metrics area under the curve (AUC) of receiver operating characteristic (ROC) curves, p-value and q-value were calculated to evaluate univariate models or parameters. For multivariable modelling using ten-fold cross-validation for model's validation, evaluation parameters, including AUC, accuracy, F1 score, precision, and recall were calculated.

3. Results

3.1. Univariate analysis

The highest AUC value was achieved for the Maximum 2D diameter slice (M2DS) shape feature (AUC = 0.88, q-value = 1.02E-7), while the average of univariate AUCs was 0.62 ± 0.08. Table 2 summarizes the AUC, p-value, q-value and mean ± SD of high AUC radiomic features after elimination of highly correlated features ($R^2 > 0.80$). It can be seen that p-values and q-values are smaller than 0.01 (except for energy), which highlights the potential of radiomic features in differentiating between MI and normal cases. The mean ± SD report the original values of radiomic features extracted from Cine-CMR, hence enabling the comparison with original values for MI and normal cases. These measures for M2DS, the best univariate feature, are 87.7 ± 9.30 for MI and 76.1 ± 5.28 for normal cases with a p-value of 1.02E-8. Yet, in Fig. 3 we used box plots of the z-score of the features to visualize differences between MI and normal cases.

M2DS from shape, Small Area Low Gray Level Emphasis (SALGLE) from GLSZM and Minimum from FO showed the highest AUC (0.88, 0.78 and 0.78, respectively) in differentiating MI from normal cases in univariate analysis. Fig. 4 shows an example of radiomics texture feature map with high rank (using MSVM-RFE) in differentiating MI from normal cardiac cases. Cine-CMR slices can be seen in the left column of the figure, while their corresponding feature maps are shown in the following columns. These feature maps with high MSVM-RFE ranking, including joint entropy, max probability, sum entropy, joint energy features from GLCM and RLNU from GLRLM were displayed in this figure. The first two rows of the image show Cine-CMR slices with feature maps of two normal cases, while the second two rows display Cine-CMR slices of two MI cases.

The different feature maps present different characteristics of cardiac tissue. This difference is strongly highlighted between two studied groups, since an obvious non-homogeneous pattern can be seen in the MI cases, whereas normal cases feature maps represent less changes in the pattern. In this figure, we depict only one slice even though the feature maps were extracted in 3D. Fig. 5 compares the results of feature maps for MI cases with the corresponding scar tissue VOI mask of LGE-CMR images. Cine-CMR slices of four MI cases, their corresponding LGE-CMR slices and the labeled LGE-CMR slices are illustrated in the first (left), second (middle) and third (right) column of the figure, respectively. The same features, as described above, are reported in this figure to show their capability in recognizing MI tissue. An approximate correspondence can be seen between the patterns represented by the feature maps and the area delineated as MI label in the third column.

3.2. Multivariate analysis

The top selected features obtained by the MSVM algorithm are presented in Table 3 . These features include one intensity-based feature (robust mean absolute deviation), one shape-based feature (surface area) and eleven texture-based features (joint entropy, maximum

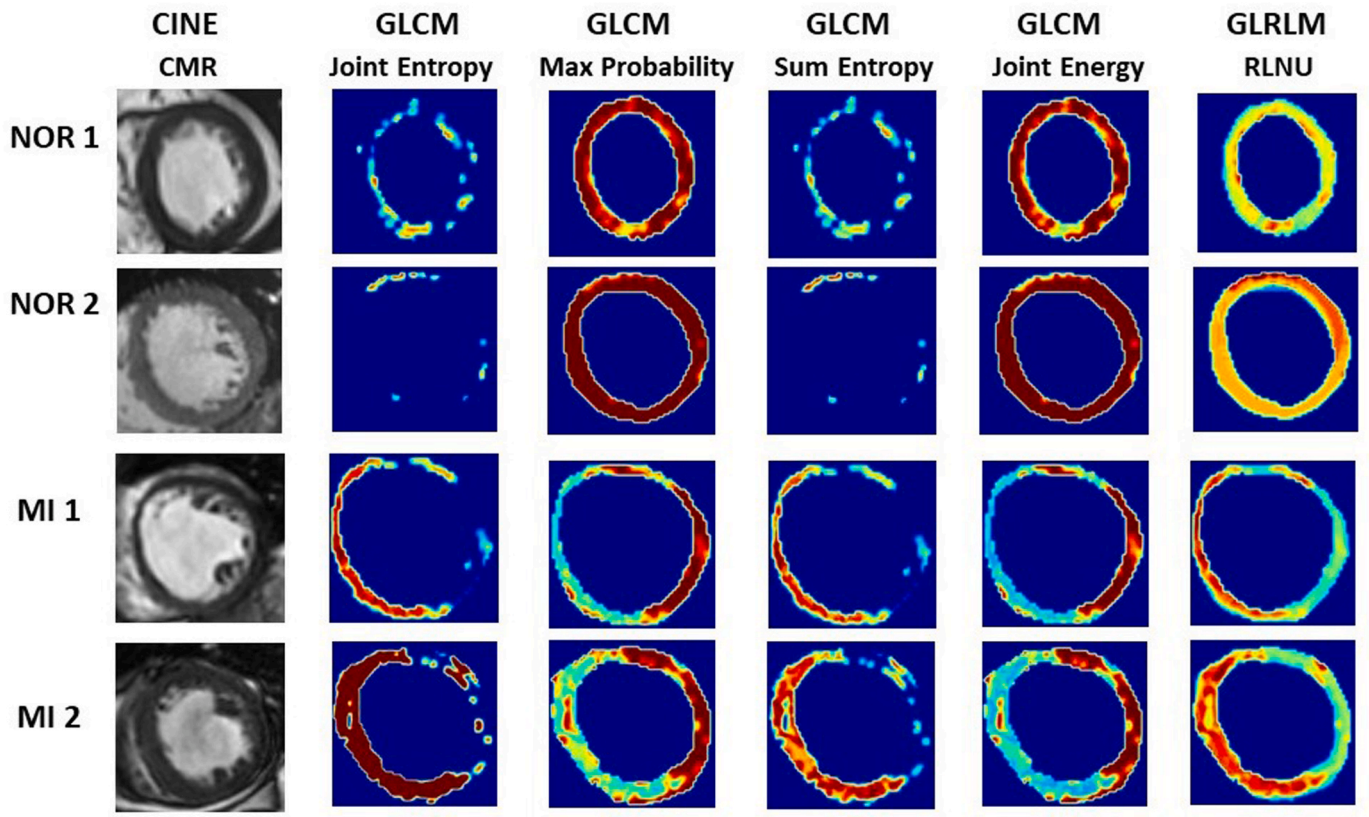

Fig. 4. Example of radiomics feature map with high MSVM-RFE ranking in differentiating MI and normal cardiac cases. Cine-CMR (first column) and different radiomics feature maps.

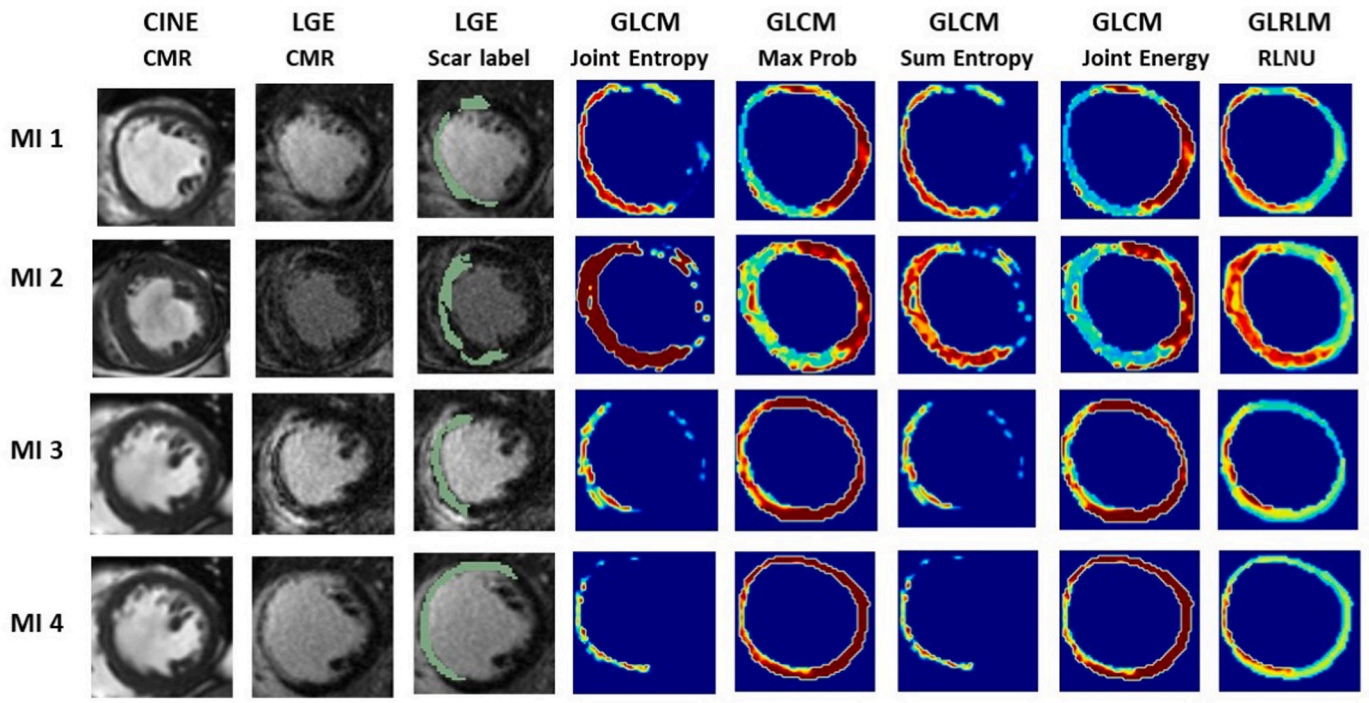

Fig. 5. Example of radiomics feature with high ranking (using MSVM-RFE) in representing scar tissue maps in different clinical studies based on LGE-CMR scar labels. Cine-CMR slices of four MI cases, with their corresponding LGE-CMR slices and the labeled LGE-CMR slices in the first (left), second (middle) and third (right) columns of the figure, along with radiomics feature maps.

Table 3
Top selected features using MSVM-RFE ranking.

Rank	Feature's Name	Type
1	Surface Area	Shape
2	Small Area Low Gray Level Emphasis	GLSZM
3	Joint Entropy	GLCM
4	Robust Mean Absolute Deviation	FO
5	Maximum Probability	GLCM
6	Sum Entropy	GLCM
7	Large Area High Gray Level Emphasis	GLSZM
8	Zone Percentage	GLSZM
9	Joint Energy	GLCM
10	Cluster Shade	GLCM
11	Run Length Non-Uniformity	GLRLM
12	Coarseness	NGTDM
13	Busyness	NGTDM

Table 4 summarizes the calculated metrics, including AUC, accuracy, precision, recall and F1 score for different classifiers. LR (AUC = 0.93 ± 0.03, Accuracy = 0.86 ± 0.05, Recall = 0.87 ± 0.1, Precision = 0.93 ± 0.03 and F1 Score = 0.90 ± 0.04) and SVM (AUC = 0.92 ± 0.05, Accuracy = 0.85 ± 0.04, Recall = 0.92 ± 0.01, Precision = 0.88 ± 0.04 and F1 Score = 0.90 ± 0.02) yielded the best performance. Fig. 6 presents the AUC, accuracy, precision and recall of machine learning algorithms.

probability, sum entropy, joint energy, and cluster shade from GLCM, small area low gray level emphasis, large area high gray level emphasis and zone percentage related to GLSZM, run length non-uniformity from GLRLM and coarseness and busyness from NGTDM).

4. Discussion

In this study, we investigated the capability of non-contrast Cine-CMR in MI diagnosis using radiomics analysis and machine learning algorithms. The univariate method using a single radiomic feature produced the highest AUC (0.88) for the M2DS feature. An average AUC of 0.62 ± 0.08 was obtained for all univariate analysis techniques using radiomic features. To improve the robustness of the results, we analyzed the feasibility of radiomic features extracted from Cine-CMR images using ten different supervised algorithms to distinguish between normal and MI cardiac cases. We found that LR (AUC = 0.93 ± 0.03, Accuracy = 0.86 ± 0.05, Recall = 0.87 ± 0.1, Precision = 0.93 ± 0.03 and F1 Score = 0.90 ± 0.04) and SVM (AUC = 0.92 ± 0.05, Accuracy = 0.85 ± 0.04, Recall = 0.92 ± 0.01, Precision = 0.88 ± 0.04 and F1 Score = 0.90 ± 0.02) yielded optimal performance as the best machine learning algorithm for this radiomics analysis. These results confirmed that multivariate radiomics analysis is able to distinguish MI from healthy cases.

Two radiomic features were common between the top univariate and MSVM-RFE selected features, including Small Area Low Gray Level Emphasis (SALGLE) and Run length non-uniformity (RLNU). SALGLE is one of the GLSZM features selected as one of the top features by both MSVM-RFE and univariate methods. GLSZM represents the number of regions (group of neighboring voxels with the same intensity values), distributed over different size of regions [50]. SALGLE as GLSZM feature emphasizes on small zones with lower gray level values [50]. In CMR images, in which infarcted regions are displayed by significantly lower intensities (even detectable visually), this feature represents infarcted regions. Yet, this feature seems to differentiate between MI and normal cases even in Cine-CMR images, where infarcted regions are not visually detectable.

In addition, RLNU is classified as one of the best features in both MSVM-RFE and univariate methods, indicating its robustness in the diagnosis of MI cases. RLNU is one of the GLRLM features which represent runs distribution in the gray values and if runs were distributed equally, the value of this feature would be low [51]. Fig. 4 shows the potential capability of RLNU in finding a homogeneous pattern in normal cases as opposed to MI cases. Fig. 5 indicates that RLNU cannot only discriminate between normal and MI cases but also represents more homogeneity in the healthy part of the myocardium in MI cases [50].

In Figs. 4 and 5, we also showed 5 texture features. Entropy is one of the GLCM descriptors which clarifies the degree of randomness [50]. Joint Entropy measures the randomness of intensity values of images in a particular neighborhood [50]. Like Joint Entropy, Sum Entropy indicates the randomness in Cine-CMR images by measuring the sum of the differences between intensity values of a neighborhood [50]. It is having been shown measurement is lower for normal cases but calculates more differences of intensities in MI cases (Fig. 4). In addition, a low rate of intensity difference is shown for the healthy part of the myocardium in MI patients. Joint Energy is one of the GLCM features, which represents the myocardium tissue homogeneity [50]. In Fig. 4, we observe the homogeneous patterns of normal cases as opposed to the non-homogeneity of MI cases. In Fig. 5, we perceive that this non-homogeneity strongly separated infarcted from healthy tissues in MI cases. Maximum probability is one of the GLCM features [50], It simply indicates the most frequent pairs of intensity values that neighbor each other in the Cine-CMR images [50].

Several studies investigated the diagnostic capability of Cine-CMR images. Cetin et al. [52] analyzed more than 5000 CVD CMR images for cardiovascular risk factors assessment and showed a significant difference between control groups and CVD cases using radiomic features. A recent study performed by Schofield et al. [33] used Cine-CMR to differentiate etiologies of left ventricular hypertrophy on more than 200 patients with the aim of reducing Gd injection in CVD patients. They were able to distinguish 5 different groups of patients using 6 intensity-based features. In our study, several texture-based features were used along with intensity-based features to improve the algorithms' discriminative capability.

Larroza et al. [53] investigated how Cine-CMR texture features could be used as indicators for differentiating MI from normal tissues. They reported that texture features extracted from Cine-CMR images could detect MI tissues, which may be applied in the detection of the infarcted myocardium as a Gadolinium-free approach. In another study by Larroza et al. [36], normal tissue was differentiated from MI through applying non-linear support vector machine on images of ten patients. Overall, 122 variables were first extracted, then the top 17 variables were used to train the non-linear support vector machine algorithm, reporting an accuracy of 0.95.

Table 4
Area under the curve (AUC), accuracy, precision, recall and F1 score for each multivariate analysis algorithm.

Method	AUC	Accuracy	Precision	Recall	F1 score
RF	0.83 ± 0.05	0.82 ± 0.04	0.84 ± 0.03	0.92 ± 0.08	0.88 ± 0.03
ET	0.70 ± 0.05	0.70 ± 0.08	0.85 ± 0.01	0.70 ± 0.14	0.76 ± 0.09
LR	0.93 ± 0.03	0.86 ± 0.05	0.93 ± 0.03	0.87 ± 0.10	0.90 ± 0.04
LDA	0.90 ± 0.05	0.82 ± 0.07	0.90 ± 0.05	0.84 ± 0.12	0.86 ± 0.06
QDA	0.76 ± 0.04	0.82 ± 0.04	0.86 ± 0.04	0.90 ± 0.08	0.87 ± 0.03
AB	0.86 ± 0.05	0.82 ± 0.07	0.85 ± 0.05	0.90 ± 0.05	0.88 ± 0.04
KNN	0.80 ± 0.05	0.74 ± 0.07	0.77 ± 0.04	0.90 ± 0.05	0.83 ± 0.04
NB	0.77 ± 0.09	0.67 ± 0.08	0.90 ± 0.10	0.63 ± 0.11	0.73 ± 0.07
SVM	0.92 ± 0.05	0.85 ± 0.04	0.88 ± 0.04	0.92 ± 0.01	0.90 ± 0.02
MLP	0.89 ± 0.09	0.84 ± 0.05	0.89 ± 0.03	0.89 ± 0.03	0.89 ± 0.03

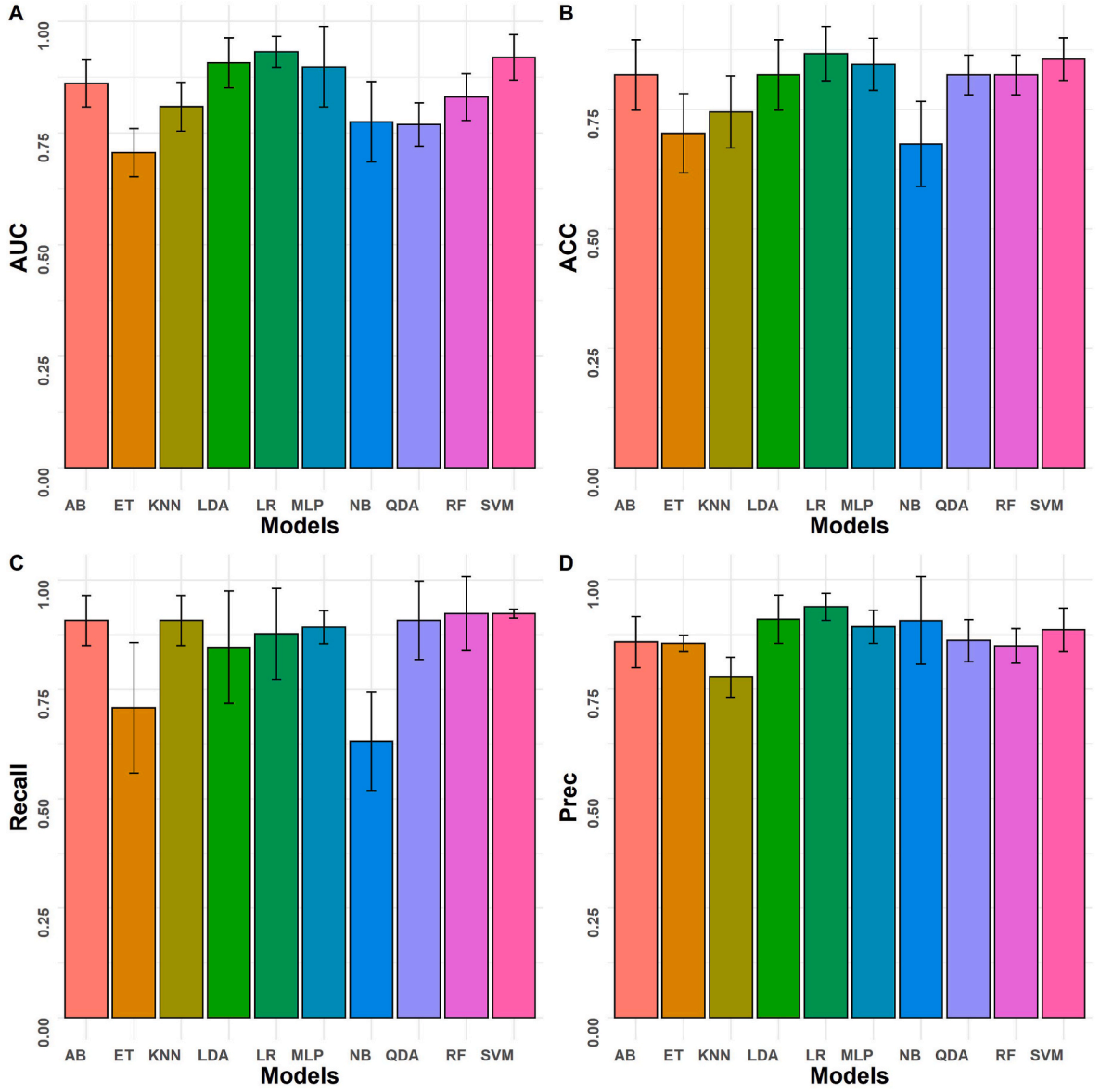

Fig. 6. Comparison of average A) AUC, B) Accuracy, C) Recall and D) Precision of various multivariate analysis methods.

A wide range of studies exploited LGE-CMR images to evaluate MI patients. Zhang et al. [16] trained a deep learning algorithm on 300 MI patients with LGE-CMR and Cine-CMR images to determine the presence and location of MI tissue and to delineate it on Cine-CMR images. Baessler et al. [15] applied radiomics analysis to evaluate and differentiate between acute and chronic MI tissues. Their aim was to demonstrate the ability of non-contrast Cine-CMR images in MI diagnosis. They examined LGE-CMR and Cine-CMR images of 120 patients and selected 5 features from 286 extracted features using the random forest algorithm. After applying logistic regression, an AUC of 0.93 was obtained for Cine-CMR, indicating the high potency of Cine-CMR in MI tissue discrimination. In a similar study conducted by Di Noto et al. [35], LGE-CMR images were used to differentiate MI tissues from myocardial edema. They extracted 563 and 933 features from 2D and 3D segmented images, respectively, and showed that the features extracted from 2D segmented images with a support vector machine classification resulted in higher accuracy (0.88) compared to 3D segmentation (0.85). More recently, Avard et al. [54] trained SVM and RF algorithms to differentiate between MI and normal tissues using LGE-CMR. They specifically achieved their aim using a small dataset consisting of 42 MI patients.

In the current study, we aimed to demonstrate the capability of radiomic features and machine learning algorithms in discriminating MI from normal cases. Using Cine-CMR radiomic features could potentially decrease Gd injection and increase the accuracy of MI detection from MR images. Clinical routine segmentation algorithms rely mainly on the intensity of images. However, we determined the radiomic features enabling to accurately detect MI tissue from unenhanced Cine-CMR (the performance of these features was improved by machine learning algorithms). In addition, the methodology followed in this work could be combined with an automated segmentation algorithm, which divides the myocardium into different segments to classify each segment apart for detecting the MI tissue in the myocardium. The feature map of univariate radiomic features could be used as a tool to detect MI regions in the myocardium. The small sample size with no external validation dataset is one of the limitations of the current study. Future work will assess the proposed model using a larger size of the external validation set. Most radiomics studies have been conducted based on manual segmentation. Furthermore, in some radiomics studies, the robustness of segmentations (both manual and automatic) were studied and manual segmentation was considered as ground truth [55–57]. Deep

learning-based radiomics analysis was suggested as a new method for radiomics analysis, an end-to-end process that does not require segmentation, feature extraction and data analysis. In this work, we used only one cardiac cycle (end diastolic) as all segmentations were performed manually by cardiac imaging experts. The segmentation of different cardiac cycles is time-consuming and labor intensive. Further studies should focus on using deep learning-based cardiac segmentation to exploit the different cycles of cardiac features for radiomics feature extraction.

5. Conclusion

In univariate analysis, M2DS from shape, SALGLE from GLSZM and Minimum from FO showed the highest performance in differentiating MI and normal cases. In addition, in multivariate analysis, LR and SVM yielded optimal results as the best machine learning algorithms for this radiomics analysis study. This work showed that using radiomics on Cine-CMR images is helpful to accurately discriminate between MI and viable tissues/normal cases, and as such, could potentially be used as an alternative to LGE-CMR in MI patients.

Declaration of competing interest

 All authors have participated in (a) conception and design, or analysis and interpretation of the data; (b) drafting the article or revising it critically for important intellectual content; and (c) approval of the final version.

 The Article I have submitted to the journal for review is original, has been written by the stated authors and has not been published elsewhere.

 The Images that I have submitted to the journal for review are original, was taken by the stated authors, and has not been published elsewhere.

 This manuscript has not been submitted to, nor is under review at, another journal or other publishing venue.

 The authors have no affiliation with any organization with a direct or indirect financial interest in the subject matter discussed in the manuscript.

 The below authors have affiliations with organizations with direct or indirect financial interest in the subject matter discussed in the manuscript:

Acknowledgements

This work was supported by the Shahid Beheshti University of Medical Sciences under grant number IR.SBMU.MSP.REC.1398.811 and the Swiss National Science Foundation under grant SNRF 320030_176052.

Appendix A. Supplementary data

Supplementary data to this article can be found online at https://doi.org/10.1016/j.compbiomed.2021.105145.

References

[1] S.S. Virani, A. Alonso, H.J. Aparicio, E.J. Benjamin, M.S. Bittencourt, C. W. Callaway, A.P. Carson, A.M. Chamberlain, S. Cheng, F.N. Delling, M.S.V. Elkind, K.R. Evenson, J.F. Ferguson, D.K. Gupta, S.S. Khan, B.M. Kissela, K.L. Knutson, C. D. Lee, T.T. Lewis, J. Liu, M.S. Loop, P.L. Lutsey, J. Ma, J. Mackey, S.S. Martin, D. B. Matchar, M.E. Mussolino, S.D. Navaneethan, A.M. Perak, G.A. Roth, Z. Samad, G.M. Satou, E.B. Schroeder, S.H. Shah, C.M. Shay, A. Stokes, L.B. VanWagner, N. Y. Wang, C.W. Tsao, Heart disease and stroke statistics-2021 update: a report from the American heart association, Circulation 143 (2021) e254–e743.

[2] E. Pozo, J. Sanz, Imaging techniques in the evaluation of post-infarction function and scar, Rev. Esp. Cardiol. 67 (2014) 754–764.

[3] T. Martins-Marques, D.J. Hausenloy, J.P. Sluijter, L. Leybaert, H. Girao, Intercellular communication in the heart: therapeutic opportunities for cardiac ischemia, Trends Mol. Med. 27 (2021) 248–262.

[4] H. Zhou, Q. Ma, P. Zhu, J. Ren, R.J. Reiter, Y. Chen, Protective role of melatonin in cardiac ischemia-reperfusion injury: from pathogenesis to targeted therapy, J. Pineal Res. 64 (2018), e12471.

[5] L. Bolognese, A.N. Neskovic, G. Parodi, G. Cerisano, P. Buonamici, G.M. Santoro, D. Antoniucci, Left ventricular remodeling after primary coronary angioplasty: patterns of left ventricular dilation and long-term prognostic implications, Circulation 106 (2002) 2351–2357.

[6] S.G. Nekolla, A. Martinez-Moeller, A. Saraste, PET and MRI in cardiac imaging: from validation studies to integrated applications, Eur. J. Nucl. Med. Mol. Imag. 36 (2009) 121–130.

[7] K.H. Schuleri, M. Centola, K.S. Evers, A. Zviman, R. Evers, J.A.C. Lima, A.C. Lardo, Cardiovascular magnetic resonance characterization of peri-infarct zone remodeling following myocardial infarction, J. Cardiovasc. Magn. Reson. 14 (2012) 24.

[8] R.J. Kim, E. Wu, A. Rafael, E.L. Chen, M.A. Parker, O. Simonetti, F.J. Klocke, R. O. Bonow, R.M. Judd, The use of contrast-enhanced magnetic resonance imaging to identify reversible myocardial dysfunction, N. Engl. J. Med. 343 (2000) 1445–1453.

[9] C. Klein, S.G. Nekolla, F.M. Bengel, M. Momose, A. Sammer, F. Haas, B. Schnackenburg, W. Delius, H. Mudra, D. Wolfram, M. Schwaiger, Assessment of myocardial viability with contrast-enhanced magnetic resonance imaging: comparison with positron emission tomography, Circulation 105 (2002) 162–167.

[10] M.J. Ricciardi, E. Wu, C.J. Davidson, K.M. Choi, F.J. Klocke, R.O. Bonow, R. M. Judd, R.J. Kim, Visualization of discrete microinfarction after percutaneous coronary intervention associated with mild creatine kinase-MB elevation, Circulation 103 (2001) 2780–2783.

[11] A. Wagner, H. Mahrholdt, T.A. Holly, M.D. Elliott, M. Regenfus, M. Parker, F. J. Klocke, R.O. Bonow, R.J. Kim, R.M. Judd, Contrast-enhanced MRI and routine single photon emission computed tomography (SPECT) perfusion imaging for detection of subendocardial myocardial infarcts: an imaging study, Lancet 361 (2003) 374–379.

[12] E. Wu, R.M. Judd, J.D. Vargas, F.J. Klocke, R.O. Bonow, R.J. Kim, Visualisation of presence, location, and transmural extent of healed Q-wave and non-Q-wave myocardial infarction, Lancet 357 (2001) 21–28.

[13] P.H. Kuo, E. Kanal, A.K. Abu-Alfa, S.E. Cowper, Gadolinium-based MR contrast agents and nephrogenic systemic fibrosis, Radiology 242 (2007) 647–649.

[14] H. Liu, L. Yan, G.S. Ma, L.P. Zhang, M. Gao, Y.L. Wang, S.P. Wang, B.C. Liu, Association of chronic kidney disease and coronary artery disease in 1,010 consecutive patients undergoing coronary angiography, J. Nephrol. 25 (2012) 219–224.

[15] B. Baessler, M. Mannil, S. Oebel, D. Maintz, H. Alkadhi, R. Manka, Subacute and chronic left ventricular myocardial scar: accuracy of texture analysis on nonenhanced cine MR images, Radiology 286 (2018) 103–112.

[16] N. Zhang, G. Yang, Z. Gao, C. Xu, Y. Zhang, R. Shi, J. Keegan, L. Xu, H. Zhang, Z. Fan, D. Firmin, Deep learning for diagnosis of chronic myocardial infarction on nonenhanced cardiac cine MRI, Radiology 291 (2019) 606–617.

[17] M. Amini, M. Nazari, I. Shiri, G. Hajianfar, M.R. Deevband, H. Abdollahi, H. Arabi, A. Rahmim, H. Zaidi, Multi-level multi-modality (PET and CT) fusion radiomics: prognostic modeling for non-small cell lung carcinoma, Phys. Med. Biol. 66 (2021).

[18] Z. Khodabakhshi, S. Mostafaei, H. Arabi, M. Oveisi, I. Shiri, H. Zaidi, Non-small cell lung carcinoma histopathological subtype phenotyping using high-dimensional multinomial multiclass CT radiomics signature, Comput. Biol. Med. 136 (2021), 104752.

[19] Z. Khodabakhshi, M. Amini, S. Mostafaei, A. Haddadi Avval, M. Nazari, M. Oveisi, I. Shiri, H. Zaidi, Overall survival prediction in renal cell carcinoma patients using computed tomography radiomic and clinical information, J. Digit. Imag. 34 (5) (2021) 1086–1098.

[20] M. Amini, G. Hajianfar, A.H. Avval, M. Nazari, M.R. Deevband, M. Oveisi, I. Shiri, H. Zaidi, Overall survival prognostic modelling of non-small cell lung cancer patients using positron emission tomography/computed tomography harmonised radiomics features: the quest for the optimal machine learning algorithm, Clin Oncol. 2021 Dec 3:S0936-6555(21)00433-7.

[21] R.J. Gillies, P.E. Kinahan, H. Hricak, Radiomics: images are more than pictures, They Are Data, Radiology 278 (2016) 563–577.

[22] M. Edalat-Javid, I. Shiri, G. Hajianfar, H. Abdollahi, H. Arabi, N. Oveisi, M. Javadian, M. Shamsaei Zafarghandi, H. Malek, A. Bitarafan-Rajabi, M. Oveisi, H. Zaidi, Cardiac SPECT radiomic features repeatability and reproducibility: a multi-scanner phantom study, J. Nucl. Cardiol. (2020).

[23] Y. Boucharebb, P. Moradi Khaniabadi, F. Al Kindi, H. Al Dhuhli, I. Shiri, H. Zaidi, A. Rahmim, Artificial intelligence-driven assessment of radiological images for COVID-19, Comput. Biol. Med. 136 (2021), 104665.

[24] X. Chen, M. Zhou, Z. Wang, S. Lu, S. Chang, Z. Zhou, Immunotherapy treatment outcome prediction in metastatic melanoma through an automated multi-objective delta-radiomics model, Comput. Biol. Med. 138 (2021), 104916.

[25] I. Shiri, Y. Salimi, M. Pakbin, G. Hajianfar, A. Haddadi Avval, A. Sanaat, S. Mostafaei, A. Akhavanallaf, A. Saberi, Z. Mansouri, D. Askari, M. Ghasemian, E. Sharifipour, S. Sandoughdaran, A. Sohrabi, E. Sadati, S. Livani, P. Iranpour, S. Kolahi, M. Khateri, S. Bijari, M.R. Atashzar, S.P. Shayesteh, B. Khosravi, M. R. Babaei, E. Jenabi, M. Hasanian, A. Shahhamzeh, S.Y. Foroghi Gholami, A. Mozafari, A. Teimouri, F. Movaseghi, A. Ahmari, N. Goharpey, R. Bozorgmehr, H. Shirzad-Aski, R. Mortazavi, J. Karimi, N. Mortazavi, S. Besharat, M. Afsharpad, H. Abdollahi, P. Geramifar, A.R. Radmard, H. Arabi, K. Rezaei-Kalantari, M. Oveisi, A. Rahmim, H. Zaidi, COVID-19 prognostic modeling using CT radiomic features and machine learning algorithms: analysis of a multi-institutional dataset of 14,339 patients, medRxiv (2021) 2021, 2012.2007.21267364.

[26] I. Shiri, M. Sorouri, P. Geramifar, M. Nazari, M. Abdollahi, Y. Salimi, B. Khosravi, D. Askari, L. Aghaghazvini, G. Hajianfar, A. Kasaeian, H. Abdollahi, H. Arabi, A. Rahmim, A.R. Radmard, H. Zaidi, Machine learning-based prognostic modeling using clinical data and quantitative radiomic features from chest CT images in COVID-19 patients, Comput. Biol. Med. 132 (2021), 104304.
[27] S. Shayesteh, M. Nazari, A. Salahshour, S. Sandoughdaran, G. Hajianfar, M. Khateri, A. Yaghobi Joybari, F. Jozian, S.H. Fatehi Feyzabad, H. Arabi, I. Shiri, H. Zaidi, Treatment response prediction using MRI-based pre-, post-, and delta-radiomic features and machine learning algorithms in colorectal cancer, Med. Phys. 48 (2021) 3691–3701.
[28] M. Nazari, I. Shiri, H. Zaidi, Radiomics-based machine learning model to predict risk of death within 5-years in clear cell renal cell carcinoma patients, Comput. Biol. Med. 129 (2021), 104135.
[29] H. Abdollahi, I. Shiri, M. Heydari, Medical imaging technologists in radiomics era: an alice in wonderland problem, Iran. J. Public Health 48 (2019) 184–186.
[30] N.Q.K. Le, T.N.K. Hung, D.T. Do, L.H.T. Lam, L.H. Dang, T.T. Huynh, Radiomics-based machine learning model for efficiently classifying transcriptome subtypes in glioblastoma patients from MRI, Comput. Biol. Med. 132 (2021), 104320.
[31] M.R. Salmanpour, M. Shamsaei, A. Saberi, G. Hajianfar, H. Soltanian-Zadeh, A. Rahmim, Robust identification of Parkinson's disease subtypes using radiomics and hybrid machine learning, Comput. Biol. Med. 129 (2021), 104142.
[32] I. Shiri, Y. Salimi, A. Saberi, M. Pakbin, G. Hajianfar, A. Haddadi Avval, A. Sanaat, A. Akhavanallaf, S. Mostafaei, Z. Mansouri, D. Askari, M. Ghasemian, E. Sharifipour, S. Sandoughdaran, A. Sohrabi, E. Sadati, S. Livani, P. Iranpour, S. Kolahi, B. Khosravi, M. Khateri, S. Bijari, M.R. Atashzar, S.P. Shayesteh, M. R. Babaei, E. Jenabi, M. Hasanian, A. Shahhamzeh, S.Y. Foroghi Gholami, A. Mozafari, H. Shirzad-Aski, F. Movaseghi, R. Bozorgmehr, N. Goharpey, H. Abdollahi, P. Geramifar, A.R. Radmard, H. Arabi, K. Rezaei-Kalantari, M. Oveisi, A. Rahmim, H. Zaidi, Diagnosis of COVID-19 using CT image radiomics features: a comprehensive machine learning study involving 26,307 patients, medRxiv (2021) 2021, 2012.2007.21267367.
[33] R. Schofield, B. Ganeshan, M. Fontana, A. Nasis, S. Castelletti, S. Rosmini, T. A. Treibel, C. Manisty, R. Endozo, A. Groves, J.C. Moon, Texture analysis of cardiovascular magnetic resonance cine images differentiates aetiologies of left ventricular hypertrophy, Clin. Radiol. 74 (2019) 140–149.
[34] T. Eftestøl, L. Woie, K. Engan, J.T. Kvaløy, D.W.T. Nilsen, S. Ørn, Texture Analysis to Assess Risk of Serious Arrhythmias after Myocardial Infarction, 2012 Computing in Cardiology, 2012, pp. 365–368.
[35] T. Di Noto, J. von Spiczak, M. Mannil, E. Gantert, P. Soda, R. Manka, H. Alkadhi, Radiomics for distinguishing myocardial infarction from myocarditis at late Gadolinium enhancement at MRI: comparison with subjective visual analysis, Radiology: Cardiothoracic Imag. 1 (2019), e180026.
[36] A. Larroza, M. Lopez-Lereu, J. Monmeneu, V. Bodi, D. Moratal, Texture Analysis for Infarcted Myocardium Detection on Delayed Enhancement MRI, 2017.
[37] P.G. Masci, J. Bogaert, Post myocardial infarction of the left ventricle: the course ahead seen by cardiac MRI, Cardiovasc. Diagn. Ther. 2 (2012) 113.
[38] K. Chatterjee, H. Swan, W.W. Parmley, H. Sustaita, H.S. Marcus, J. Matloff, Influence of direct myocardial revascularization on left ventricular asynergy and function in patients with coronary heart disease: with and without previous myocardial infarction, Circulation 47 (1973) 276–286.
[39] K.A. Lara Hernandez, T. Rienmüller, D. Baumgartner, C. Baumgartner, Deep learning in spatiotemporal cardiac imaging: a review of methodologies and clinical usability, Comput. Biol. Med. 130 (2021), 104200.
[40] A.M. Naderi, H. Bu, J. Su, M.H. Huang, K. Vo, R.S. Trigo Torres, J.C. Chiao, J. Lee, M.P.H. Lau, X. Xu, H. Cao, Deep learning-based framework for cardiac function assessment in embryonic zebrafish from heart beating videos, Comput. Biol. Med. 135 (2021), 104565.
[41] Q. Tong, C. Li, W. Si, X. Liao, Y. Tong, Z. Yuan, P.A. Heng, RIANet: recurrent interleaved attention network for cardiac MRI segmentation, Comput. Biol. Med. 109 (2019) 290–302.
[42] H. Cui, C. Yuwen, L. Jiang, Y. Xia, Y. Zhang, Bidirectional cross-modality unsupervised domain adaptation using generative adversarial networks for cardiac image segmentation, Comput. Biol. Med. 136 (2021), 104726.
[43] L. Xie, Y. Song, Q. Chen, Automatic left ventricle segmentation in short-axis MRI using deep convolutional neural networks and central-line guided level set approach, Comput. Biol. Med. 122 (2020), 103877.
[44] A. Fedorov, R. Beichel, J. Kalpathy-Cramer, J. Finet, J.C. Fillion-Robin, S. Pujol, C. Bauer, D. Jennings, F. Fennessy, M. Sonka, J. Buatti, S. Aylward, J.V. Miller, S. Pieper, R. Kikinis, 3D slicer as an image computing platform for the quantitative imaging network, Magn. Reson. Imaging 30 (2012) 1323–1341.
[45] N.J. Tustison, B.B. Avants, P.A. Cook, Y. Zheng, A. Egan, P.A. Yushkevich, J.C. Gee, N4ITK: improved N3 bias correction, IEEE Trans Med Imaging 29 (2010) 1310–1320.
[46] J.J.M. van Griethuysen, A. Fedorov, C. Parmar, A. Hosny, N. Aucoin, V. Narayan, R.G.H. Beets-Tan, J.C. Fillion-Robin, S. Pieper, H. Aerts, Computational radiomics system to decode the radiographic phenotype, Cancer Res. 77 (2017) e104–e107.
[47] R.J. Gillies, P.E. Kinahan, H. Hricak, Radiomics: images are more than pictures, they are data, Radiology 278 (2016) 563–577.
[48] X. Zhou, D.P. Tuck, MSVM-RFE: extensions of SVM-RFE for multiclass gene selection on DNA microarray data, Bioinformatics 23 (2007) 1106–1114.
[49] V. Pedregosa F, el Ga", A. Gramfort, V. Michel, B. Thirion, O. Grisel, et al., Scikit-learn: machine learning in Python, J. Mach. Learn. Res. 12 (2011) 2825–2830.
[50] A. Zwanenburg, S. Leger, M. Vallières, S. Löck, f. Initiative, Image Biomarker Standardisation Initiative - Feature Definitions, 2016.
[51] M.M. Galloway, Texture analysis using grey level run lengths, NASA STI/Recon Tech. Rep. N 75 (1974), 18555.
[52] I. Cetin, Z. Raisi-Estabragh, S.E. Petersen, S. Napel, S.K. Piechnik, S. Neubauer, M. A. Gonzalez Ballester, O. Camara, K. Lekadir, Radiomics signatures of cardiovascular risk factors in cardiac MRI: results from the UK biobank, Front Card. Med. 7 (2020), 591368.
[53] A. Larroza, M.P. Lopez-Lereu, J.V. Monmeneu, J. Gavara, F.J. Chorro, V. Bodi, D. Moratal, Texture analysis of cardiac cine magnetic resonance imaging to detect nonviable segments in patients with chronic myocardial infarction, Med. Phys. 45 (2018) 1471–1480.
[54] E. Avard, I. Shiri, G. Hajianfar, H. Abdollahi, K. Kasani, K.R. Kalantari, A. Bitarafan-Rajabi, M.R. Deevband, M. Oveisi, H. Zaidi, Late Gadolinium enhanced cardiac magnetic resonance imaging radiomics for high precision differentiation of scar and viable cardiac tissues, IEEE Nucl. Sci. Symp. Med. Imag. Conf. (NSS/MIC) (2020) 1–4.
[55] S. Huang, J. Liu, L.C. Lee, S.K. Venkatesh, L.L. San Teo, C. Au, W.L. Nowinski, An image-based comprehensive approach for automatic segmentation of left ventricle from cardiac short axis cine mr images, J. Digit. Imag. 24 (2011) 598–608.
[56] S. Queirós, D. Barbosa, B. Heyde, P. Morais, J.L. Vilaça, D. Friboulet, O. Bernard, J. D'hooge, Fast automatic myocardial segmentation in 4D cine CMR datasets, Med. Image Anal. 18 (2014) 1115–1131.
[57] A. Budai, F.I. Suhai, K. Csorba, A. Toth, L. Szabo, H. Vago, B. Merkely, Fully automatic segmentation of right and left ventricle on short-axis cardiac MRI images, Comput. Med. Imag. Graph. 85 (2020), 101786.